Geomechanics and Engineering, *Vol. 36, No. 1 (2024) 83-97*
https://doi.org/10.12989/gae.2024.36.1.083

Prediction of the long-term deformation of high rockfill geostructures using a hybrid back-analysis method

Ming Xu* and Dehai Jin[a]

Department of Civil Engineering, Tsinghua University, Beijing 100084, China

(*Received March 9, 2023, Revised December 1, 2023, Accepted December 5, 2023*)

Abstract. It is important to make reasonable prediction about the long-term deformation of high rockfill geostructures. However, the deformation is usually underestimated using the rockfill parameters obtained from laboratory tests due to different size effects, which make it necessary to identify parameters from in-situ monitoring data. This paper proposes a novel hybrid back-analysis method with a modified objective function defined for the time-dependent back-analysis problem. The method consists of two stages. In the first stage, an improved weighted average method is proposed to quickly narrow the search region; while in the second stage, an adaptive response surface method is proposed to iteratively search for the satisfactory solution, with a technique that can adaptively consider the translation, contraction or expansion of the exploration region. The accuracy and computational efficiency of the proposed hybrid back-analysis method is demonstrated by back-analyzing the long-term deformation of two high embankments constructed for airport runways, with the rockfills being modeled by a rheological model considering the influence of stress states on the creep behavior.

Keywords: adaptive response surface method; back-analysis; improved weighted average method; long-term deformation; rockfill; size effect

1. Introduction

Rockfills have been widely used in the construction of high embankments in mountain areas for transportation infrastructures, e.g., airports, high-speed railways, and highways (Soriano and Sanchez 1999, Nagahara *et al.* 2004, Xu *et al.* 2009, 2017, Canizal *et al.* 2015, Yao *et al.* 2018, 2020). Rockfills have also been used in the construction of concrete face rockfill dams (Zhou *et al.* 2016, Kermani *et al.* 2017, Qin *et al.* 2020) and clay-core rockfill dam (Nasiri *et al.* 2020). Because these high rockfill geostructures are sensitive to deformation in the service life, it is important to make reasonable predictions regarding the long-term deformation.

Rockfills exhibit many complex mechanical properties, including nonlinear stress–strain behavior, stress-dependent behavior, and time-dependent behavior, as demonstrated in previous laboratory investigations utilizing large-scale testing equipments (Anhdan *et al.* 2006, Charles 2008, Xu *et al.* 2009, 2012, Alonso *et al.* 2016). The finite element method (FEM) and finite difference method (FDM) have been adopted to predict the deformation of high-fill geostructures, with parameters derived from laboratory testing. However, it is well recognized that the predicted long-term deformation using the parameters of rockfill measured in the laboratory is usually seriously underestimated compared with that measured in the field (Frossard *et al.* 2012, Zhou *et al.* 2019, Sukkarak *et al.* 2018). Furthermore, the predicted long-term settlement becomes approximately stable much quicker than the field observation (Xu *et al.* 2019).

The possible reason for such divergence can be attributed to the size effect. There are at least four different size effects:

1) Grain size effect. Because the dimension of the testing apparatus is always limited, the maximum grain size of rockfill adopted in the laboratory has to be much smaller than that in the field. However, larger rockfill particles contain more and larger microcracks, resulting in lower particle strengths (Lee 1992, Mcdowel and Bolton 1998, Alonso *et al.* 2012). As a sequence, specimens with larger particles were found to exhibit a lower friction angle and larger volumetric compression (Hu *et al.* 2011, Tapias *et al.* 2015), as well as more significant creep (Rahmania and Panah 2020).

2) Size effect of particle size distribution. In the laboratory, the density of rockfill is usually specified as the same as that in the field. However, the particle size distribution has to be scaled down from that in the field, resulting in different relative density, which might bring very different mechanical behavior.

3) Time size effect. The creep parameters of rockfill are usually derived from large triaxial creep test or large oedometer creep test in the laboratory, in which the loading period before the creep stage is much shorter than the construction period in the field. Hong and Xu (2021) reveals that this difference in loading period would contribute to the underestimation of the long-term settlement of high rockfill geostructures.

4) Structure size effect. Song *et al.* (2018) carried out

*Corresponding author, Associate Professor
E-mail: mingxu@mail.tsinghua.edu.cn
[a]Ph.D. Student

ISSN: 2005-307X (Print), 2092-6219 (Online)

finite element analysis on the deformation of embankments with different heights. They found that variability of the mechanical properties of rockfills, particularly variation in parameters related to plastic deformation, could also lead to underestimation of the deformation of high embankment.

An underestimation of the long-term settlement would lead to unsafe design and operation of high rockfill geostructures, while it seems impossible at the current stage to avoid these different size effects in the laboratory using the available testing apparatus and techniques. Therefore, it becomes necessary to perform back-analysis to identify parameters based on the field monitoring data.

To solve the parameter identification (PI) problem, an objective function and convergence tolerance (F_{ct}) is usually desired. The objective function is used to describe the difference between the in-situ monitoring data and the corresponding numerical results. F_{ct} is used to judge whether the result of the PI is satisfactory. The objective function is usually defined (Pichler *et al.* 2003) as

$$F(\mathbf{p}) = \sqrt{\frac{1}{n_0}\sum_{r=1}^{n_0}\left(\frac{u_r^h(\mathbf{p}) - u_r}{u_r}\right)^2} \tag{1}$$

where u_r and $u_r^h(\mathbf{p})$ are the field data and the corresponding calculated results, respectively. Here, $\mathbf{p}=[p_1, p_2, ..., p_k]^{\mathrm{T}}$ is a $(k\times 1)$ vector, which collects the unknown model parameters. To find a satisfactory solution (i.e., $F(\mathbf{p}) < F_{ct}$), various techniques have been proposed in the literature. These techniques can be generally divided into two categories: gradient-free PI methods and gradient-based PI methods.

The gradient-free PI method searches for the satisfactory solution within the entire parameter space by employing approaches such as genetic algorithms, stochastic search techniques, etc. (e.g., Wang *et al.* 2007, Behnia *et al.* 2013, Zhou *et al.* 2022). Hence, this method is highly powerful in solving nonlinear optimization problems. However, a large number of numerical samples are usually required in the gradient-free PI method, leading to computational inefficiency, especially when the problem is simple or mathematically well behaved. The gradient-based PI method iteratively searches the minimum value of the objective function by employing the gradient of $F(\mathbf{p})$ (e.g., Ledesma *et al.* 1996, Calvello and Finno 2004, Finno and Calvello 2005, Park and Park 2015). This method can improve calculation efficiency to reduce computing time. However, the gradient-based PI method searches for the satisfactory solution in a local parameter space and might become trapped at a local optimal solution.

The response surface method (RSM) is an effective gradient-based PI method, which has been widely used in the field of chemistry and chemical industry (Sarabia and Ortiz 2020). In the back-analysis procedure, mathematical expressions between the considered responses (e.g., the displacements of the key monitoring locations) and the unknown model parameters are established first. Then, the objective function (i.e., the difference between the calculated responses and those observed in-situ) is expressed as a function of these parameters. The satisfactory solution can be obtained using different optimization algorithms. In recent years, RSM began to be employed to solve back-analysis problems in geotechnical engineering (e.g., Park and Park 2015, Zhao *et al.* 2015).

However, further improvement is desired to use the response surface method in the prediction of the long-term deformation of high rockfill geostructures. The objective function in Eq. (1) cannot consider the weight of monitoring time. The first exploration region of parameters for constructing the response surface is usually subjectively determined by the designers. If the exploration region is far away from the optimal region, the fitted responses might be very different from the real responses, resulting in a slow convergence rate. Furthermore, the size of exploration region is usually kept unchanged in subsequent iterations, which also leads to low efficiency.

This paper proposes a hybrid back-analysis method for prediction about the long-term deformation of high rockfill geostructures. A modified objective function is defined for the time-dependent back-analysis problem. In the first stage, an improved weighted average method is proposed to quickly narrow the search region. In the second stage, an adaptive response surface method is proposed to iteratively search for the satisfactory solution, with a technique that can adaptively consider the translation, contraction or expansion of the exploration region. The accuracy and computational efficiency of the proposed hybrid back-analysis method is demonstrated by back-analyzing the long-term deformation of two high rockfill embankments.

2. Hybrid back-analysis method for long-term deformation prediction

A new objective function is proposed to consider the weight of monitoring time in Section 2.1. Then the hybrid back-analysis method is described in Section 2.2, including two stages, i.e., the improved weighted average method (Stage 1) and the adaptive response surface method (Stage 2).

2.1 Objective function for the time-dependent back-analysis problem

An objective function is formulated for the time-dependent back-analysis problem as

$$F(\mathbf{p}) = \sum_{r=1}^{m}\sum_{s=1}^{l} w_{rs}\sqrt{\left(\frac{u_{rs}^h(\mathbf{p}, t_s) - u_r(t_s)}{u_r(t_s)}\right)^2} \tag{2}$$

where $\mathbf{p}=[p_1, p_2, ..., p_k]^{\mathrm{T}}$ is a $(k\times 1)$ vector of the unknown parameters; $u_r(t_s)$ is the measured deformation of location r at time s; and $u_{rs}^h(\mathbf{p}, t_s)$ is the corresponding calculated deformation when the vector $\mathbf{p}$ is input into the numerical analysis. m and l are the numbers of the monitoring locations and time points for the back analysis, respectively.

w_{rs} is the weighting coefficient of the monitoring location *r* at time *s*, and is defined as

$$w_{rs} = t_s / \left(m \sum_{s=1}^{l} t_s \right) \tag{3}$$

where t_s is the actual value at time *s*. According to Eq. (3), a greater value of t_s leads to a greater value of w_{rs}, which means the importance of the in-situ monitoring data increases with the monitoring time.

2.2 Hybrid back-analysis method

2.2.1 Stage 1: Improved weighted average method

The weighted average method was originally proposed by Guan *et al*. (2008), which can quickly identify an initial optimal solution at the initial region. However, this approach is not able to conduct further search for the better solution if the initial optimal solution is not satisfactory. Thus, the method is improved to quickly narrow the search region and determine the first exploration region for the next stage. The improved weighted average method includes the following four steps.

Step 1: Creating the calculation samples

The parameters that need to be identified are collected in the $(k\times1)$ vector $\mathbf{p}=\left[p_1, p_2, ..., p_k\right]^{\mathrm{T}}$. The initial region is usually determined based on engineering experience and expressed as $\left[\mathbf{p}_{\mathrm{c}}^{(0)}-\Delta\mathbf{p}^{(0)}, \mathbf{p}_{\mathrm{c}}^{(0)}+\Delta\mathbf{p}^{(0)}\right]$. Here, $\mathbf{p}_{\mathrm{c}}^{(0)}=[p_{1,\mathrm{c}}^{(0)}, \cdots, p_{k,\mathrm{c}}^{(0)}]^{\mathrm{T}}$ is the center of this region, and $\Delta\mathbf{p}^{(0)}=\left[\Delta p_1^{(0)}, \cdots, \Delta p_k^{(0)}\right]^{\mathrm{T}}$ is a $(k\times1)$ vector collecting the range of each parameter. The subscript c denotes the center of the exploration region and the superscript (0) denotes the initial condition. Therefore, the calculation samples contain the following locations:

1) the vertex of the initial region (2k): $[p_{1,\mathrm{c}}^{(0)} \pm \Delta p_1^{(0)}, \cdots, p_{k,\mathrm{c}}^{(0)} \pm \Delta p_k^{(0)}]$

2) the surface center of the initial region (2k): $[p_{1,\mathrm{c}}^{(0)}, \cdots, p_{i,\mathrm{c}}^{(0)} \pm \Delta p_i^{(0)}, \cdots, p_{k,\mathrm{c}}^{(0)}]$

3) the center of the initial region $\mathbf{p}_c^{(0)}=\left[p_{1,c}^{(0)}, \cdots, p_{k,c}^{(0)}\right]$ (1):

Overall, the number of calculation samples is $N=2^k+2k+1$.

Step 2: Calculating the weight u_i of each calculation sample

The numerical results of the above *N* calculation samples can be obtained by adopting the corresponding model parameters of each sample in numerical analysis. With the results and in-situ monitoring data, the $F(\mathbf{p})$ value of each calculation sample is obtained according to Eq. (2), which reflects the difference between the input parameters and the satisfactory solution. Guan *et al*. (2008) defined the weight u_i of each sample as

$$u_i = \frac{1/F\left(\mathbf{p}_i\right)}{\sum_{i=1}^{N} 1/F\left(\mathbf{p}_i\right)} \qquad i=1, \cdots, N \tag{4}$$

where $\mathbf{p}_i$ is the ith parameter vector among the N calculation samples. As shown in Eq. (4), a greater weight u_i indicates a smaller difference between the input parameters and the satisfactory solution.

Step 3: Calculating $\mathbf{p}_{\mathrm{opt}}^{(0)}$

The optimal solution of the weighted average method is obtained via

$$\mathbf{p}_{\mathrm{opt}}^{(0)} = \sum_{i=1}^{N} u_i \mathbf{p}_i \qquad i=1, \cdots, N \tag{5}$$

The subscript opt denotes the optimal solution. $F\left(\mathbf{p}_{\mathrm{opt}}^{(0)}\right)$ is obtained according to Eq. (2). The value of the convergence tolerance F_{ct} is specified based on the scattering extent of the field monitoring data. If $F\left(\mathbf{p}_{\mathrm{opt}}^{(0)}\right) < F_{ct}$, $\mathbf{p}_{\mathrm{opt}}^{(0)}$ can be regarded as the satisfactory solution. However, it is rare to obtain the satisfactory solution at this step in practice. Thus, Step 4 is performed.

Step 4: Determining the first exploration region

Although $\mathbf{p}_{\mathrm{opt}}^{(0)}$ is not the satisfactory solution, it is much closer to that. Thus, $\mathbf{p}_{\mathrm{opt}}^{(0)}$ is used as the center of the first exploration region (i.e., $\mathbf{p}_{\mathrm{c}}^{(1)}=\mathbf{p}_{\mathrm{opt}}^{(0)}$) for the next stage. The superscript (1) denotes the first iteration. Here, the range of each parameter is formulated as

$$\Delta\mathbf{p}^{(1)} = \Delta\mathbf{p}^{(0)} \left(\frac{F\left(\mathbf{p}_{\mathrm{c}}^{(1)}\right)}{F\left(\mathbf{p}_{\mathrm{c}}^{(0)}\right)} \right) \tag{6}$$

where $\Delta\mathbf{p}^{(1)}$ and $\Delta\mathbf{p}^{(0)}$ are $(k\times1)$ vectors of the range of each parameter in the first iteration and the initial condition, respectively. $F\left(\mathbf{p}_{\mathrm{c}}^{(1)}\right)$ and $F\left(\mathbf{p}_{\mathrm{c}}^{(0)}\right)$ are the values of the objective function at the center of the exploration region in the first iteration and the initial condition, respectively. Therefore, the improved weighted averaged method can provide the first exploration region for the next stage as $\left[\mathbf{p}_{\mathrm{c}}^{(1)}-\Delta\mathbf{p}^{(1)}, \mathbf{p}_{\mathrm{c}}^{(1)}+\Delta\mathbf{p}^{(1)}\right]$, the dimension of which becomes much smaller than the initial region.

2.2.2 Stage 2: adaptive response surface method

The classical RSM is usually implemented by the first-order analysis, the steepest descent analysis and the second-order analysis. The first two steps continue until the exploration region move to the vicinity of optimal region. However, the searching size of the two steps is subjectively determined by the designers, which may result in searching inefficiency. Furthermore, the size of exploration region is usually kept unchanged in subsequent iterations, which also cause low efficiency.

To produce a faster convergence rate, an adaptive RSM is proposed in this subsection. The relation between the objective function and the unknown model parameters is directly estimated using a second-order polynomial as

$$F^{(m)}(\mathbf{p}) = \beta_0^{(m)} + \sum_{1}^{k} \beta_i^{(m)} p_i + \sum_{1}^{k} \beta_{ii}^{(m)} p_i^2 + \sum_i \sum_j \beta_{ij}^{(m)} p_i p_j \tag{7}$$

where $\mathbf{p}=[p_1, p_2,..., p_k]^{\mathrm{T}}$ is a $(k\times1)$ vector. p_i and p_j are the ith and jth parameters in vector $\mathbf{p}$, respectively. $\beta_0^{(m)}$, $\beta_i^{(m)}$, $\beta_{ii}^{(m)}$ and $\beta_{ij}^{(m)}$ are the coefficients of constant term, p_i, p_i^2 and $p_i p_j$ in the mth iteration, respectively. The size of exploration region can be automatically adjusted according to the $F(\mathbf{p})$ values at the center of the exploration region in the current and previous iterations. The adaptive RSM method consists of the following four steps.

Step 1: Determining the exploration region in the mth iteration

The optimal solution in the *(m-1)*th iteration is regarded as the center of the exploration region in the mth iteration (i.e., $\mathbf{p}_{\mathrm{c}}^{(m)}=\mathbf{p}_{\mathrm{opt}}^{(m-1)}$). The range of each parameter in the mth iteration is formulated as

$$\Delta\mathbf{p}^{(m)}=\Delta\mathbf{p}^{(m\text{-}1)}\left(\frac{F\left(\mathbf{p}_{\mathrm{c}}^{(m)}\right)}{F\left(\mathbf{p}_{\mathrm{c}}^{(m-1)}\right)}\right) \tag{8}$$

where $\Delta\mathbf{p}^{(m)}$ and $\Delta\mathbf{p}^{(m\text{-}1)}$ are $(k\times1)$ vectors of the range of each parameter in the mth and $(m$-1)th iterations, respectively. $F\left(\mathbf{p}_{\mathrm{c}}^{(m)}\right)$ and $F\left(\mathbf{p}_{\mathrm{c}}^{(m-1)}\right)$ are the values of the objective function at the center of the exploration region in the mth and $(m$-1)th iterations, respectively. In the first iteration (m=1), Eq. (8) is equal to Eq. (6), i.e., the improved weighted average method determines the first exploration region for the adaptive RSM.

In Eq. (8), if $F\left(\mathbf{p}_{\mathrm{c}}^{(m)}\right)<F\left(\mathbf{p}_{\mathrm{c}}^{(m-1)}\right)$, $\Delta\mathbf{p}^{(m)}<\Delta\mathbf{p}^{(m\text{-}1)}$. Otherwise, $\Delta\mathbf{p}^{(m)}>\Delta\mathbf{p}^{(m\text{-}1)}$. Therefore, the exploration region can be contracted or expanded according to the $F(\mathbf{p})$ values at the center of the exploration region in the current and the previous iterations. This is the reason why we call this method an adaptive RSM.

In general, $\Delta\mathbf{p}^{(m)}<\Delta\mathbf{p}^{(m\text{-}1)}$. However, if the size of the exploration region is too small, the convergence rate will be slow. Thus, the empirical lower and upper bounds are specified as

$$0.1\Delta\mathbf{p}^{(0)}<\Delta\mathbf{p}^{(m)}<0.7\Delta\mathbf{p}^{(0)} \tag{9}$$

The exploration region in the mth iteration is $\left[\mathbf{p}_{\mathrm{c}}^{(m)}-\Delta\mathbf{p}^{(m)}, \mathbf{p}_{\mathrm{c}}^{(m)}+\Delta\mathbf{p}^{(m)}\right]$

Step 2: Creating the calculation samples

The central composite design (Oyejola and Nwanya 2015) is adopted to create the calculation samples, which contain the following locations:

1) the vertex of the region (2^k): $[p_{1,\mathrm{c}}^{(m)}\pm\Delta p_1^{(m)},\cdots, p_{k,\mathrm{c}}^{(m)}\pm\Delta p_k^{(m)}]$

2) the surface center of the region ($2k$): $[p_{1,\mathrm{c}}^{(m)},\cdots,p_{i,\mathrm{c}}^{(m)}\pm\sqrt{k}\Delta p_i^{(m)},\cdots, p_{k,\mathrm{c}}^{(m)}]$

3) the center of the region (1): $[p_{1,\mathrm{c}}^{(m)},\cdots, p_{k,\mathrm{c}}^{(m)}]$

Overall, there are $N=2^k+2k+1$ calculation samples. The numerical results of the above N calculation samples are obtained with those model parameters. Then $F(\mathbf{p})$ of each calculation sample is obtained according to Eq. (2).

Step 3: Constructing the response surface in the current iteration

Based on the $F(\mathbf{p})$ values, the coefficients in Eq. (7) can be obtained via the least squares regression. Before solving for the optimal solution, the precision of the fitted response surface needs to be investigated. A fitting tolerance (R_{fi}) is defined. If R^2 of Eq. (7) is greater than R_{fi}, Step 4 is executed. Otherwise, the exploration region is contracted to two-thirds of the current range and Step 2 is executed.

Step 4: Identifying the optimal solution in the current iteration

Eq. (7) is re-written in matrix notation as

$$F^{(m)}(\mathbf{p})=\beta_0^{(m)}+\mathbf{p}^{\mathrm{T}}\mathbf{b}^{(m)}+\mathbf{p}^{\mathrm{T}}\mathbf{B}^{(m)}\mathbf{p} \tag{10}$$

where

$$\mathbf{p}=\begin{bmatrix}p_1\\p_2\\\cdots\\p_k\end{bmatrix},\ \mathbf{b}^{(m)}=\begin{bmatrix}\beta_1^{(m)}\\\beta_2^{(m)}\\\cdots\\\beta_k^{(m)}\end{bmatrix},\ \text{and}$$

$$\mathbf{B}^{(m)}=\begin{bmatrix}\beta_{11}^{(m)} & \beta_{12}^{(m)}/2 & \cdots & \beta_{1k}^{(m)}/2\\ & \beta_{22}^{(m)} & \cdots & \beta_{2k}^{(m)}/2\\ & & \cdots & \cdots\\ \text{sym.} & & & \beta_{kk}^{(m)}\end{bmatrix}$$

$\mathbf{b}^{(m)}$ is a $(k\times1)$ vector of the linear regression coefficients, and $\mathbf{B}^{(m)}$ is a $(k\times k)$ symmetric matrix. The diagonal elements of $\mathbf{B}^{(m)}$ are the pure quadratic coefficients ($\beta_{ii}^{(m)}$) and the off-diagonal elements of $\mathbf{B}^{(m)}$ are one-half the mixed quadratic coefficients ($\beta_{ij}^{(m)}$, $i\neq j$). If the solution that optimizes the fitted response exits, it will be formulated as

$$\mathbf{p}_{\mathrm{RSM}}^{(m)}=-\frac{1}{2}\left[\mathbf{B}^{(m)}\right]^{-1}\mathbf{b}^{(m)} \tag{11}$$

where $\mathbf{p}_{\mathrm{RSM}}^{(m)}$ is a $(k\times1)$ vector. Then, the value of $F\left(\mathbf{p}_{\mathrm{RSM}}^{(m)}\right)$ can be obtained. By comparing $F\left(\mathbf{p}_{\mathrm{RSM}}^{(m)}\right)$ with $F(\mathbf{p})$ of other calculation samples, the optimal solution in the mth iteration of the adaptive RSM (i.e., $\mathbf{p}_{\mathrm{opt}}^{(m)}$) can be identified as the sample with the minimum $F(\mathbf{p})$ value. If $F\left(\mathbf{p}_{\mathrm{opt}}^{(m)}\right)<F_{ct}$, $\mathbf{p}_{\mathrm{opt}}^{(m)}$ is the satisfactory solution. Otherwise, $\mathbf{p}_{\mathrm{opt}}^{(m)}$ is selected as the center of the exploration region in the $(m$+1)th iteration (i.e., $\mathbf{p}_{\mathrm{c}}^{(m+1)}=\mathbf{p}_{\mathrm{opt}}^{(m)}$), and a new iteration is executed.

In summary, the adaptive RSM can reduce the number of fitting response surface by directly estimating the relation between the objection function and the unknown model parameters, and have a faster convergence rate by adaptively considering the translation, contraction or expansion of the exploration region. The flowchart of this method is summarized in Fig. 1.

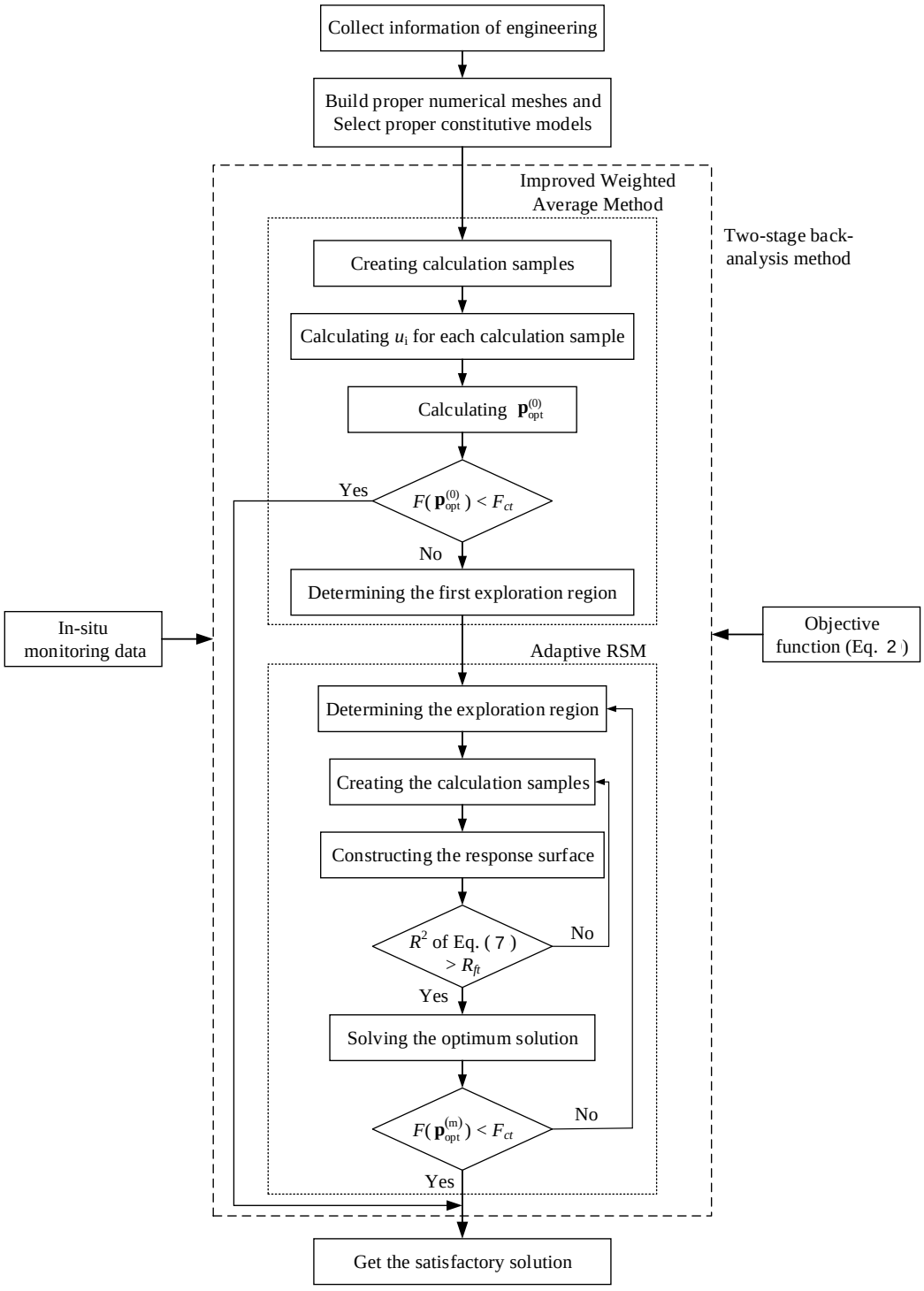

Fig. 1 Flowchart of the hybrid back-analysis method

3. Constitutive modelling of rockfills

Rockfills have been extensively used for the construction of the high rockfill embankments and dams, which exhibit complex time-dependent behavior (Charles 2008, Xu *et al*. 2009). Xu *et al*. (2018) proposed a rheological model in order to reproduce the influence of stress states (i.e., the deviator stress level and confining pressure) on the creep behavior of rockfills. The model was developed based on the classic Burgers model, as shown in Fig. 2. The total strain consists of three parts

$$\varepsilon_i = \varepsilon_i^{NE} + \varepsilon_i^{N,M} + \varepsilon_i^{K,M} \tag{12}$$

$$\varepsilon_i^{NE} = \left((1+\upsilon)\sigma_i - \upsilon\sigma_{kk}\right)/E \tag{13}$$

$$\varepsilon_i^{N,M} = q_i t / 2\eta^N \tag{14}$$

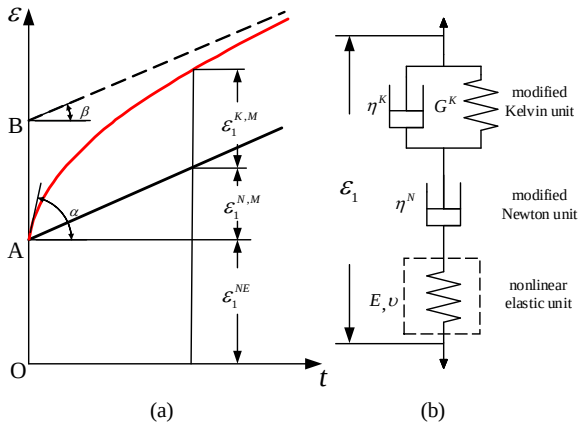

(a) (b)

Fig. 2 The rheological model for rockfills proposed by Xu *et al.* (2018): (a) the strain-time curve; and (b) the schematic view of the model

$$\varepsilon_i^{K,M} = \frac{q_i}{2G^K}\left(1-\exp(-\frac{G^K}{\eta^K}t)\right) \tag{15}$$

where ε_i^{NE}, $\varepsilon_i^{N,M}$ and $\varepsilon_i^{K,M}$ are the strains of the nonlinear elastic unit, the modified Newton unit and the modified Kelvin unit, respectively ($i=1,2,3$). σ_i is the principal stress; $\sigma_{kk}=\sigma_1+\sigma_2+\sigma_3$. q_i is the deviator stress and calculated as $q_i=\sigma_i-\sigma_{kk}/3$. Poisson's ratio ν is set to 0.3.

In order to reproduce the nonlinear stress-strain behavior, Eq. (16) is adopted to calculate E , which is similar to that adopted in the Duncan-Chang model (Duncan and Chang 1970).

$$E=\left(1-R_f\frac{1-\sin\varphi}{2\sigma_3\sin\varphi}(\sigma_1-\sigma_3)\right)^2 Kp_a\left(\frac{\sigma_3}{p_a}\right)^n \tag{16}$$

where K , n , and R_f are the tangent modulus number, tangent modulus exponent and failure ratio, respectively. p_a is the atmospheric pressure. φ is the friction angle, which is calculated by Eq. (17)

$$\varphi=\varphi_0-\Delta\varphi\log\left(\frac{\sigma_3}{p_a}\right) \tag{17}$$

where φ_0 is the value of φ for $\sigma_3=p_a$ and $\Delta\varphi$ is the reduction in φ for a 10-fold increase in σ_3.

Xu et al. (2018) reveals that the confining pressure (σ_3) and deviator stress level ($D=(\sigma_1-\sigma_3)/(\sigma_1-\sigma_3)_f$) has a substantial influence on the values of G^K, η^K and η^N of rockfills, and proposed Eqs. (18)-(20)

$$G^K=10^{K_1}p_a(\frac{\sigma_3}{p_a})^{n_1}(1-aD) \tag{18}$$

$$\eta^K=10^{K_2}\left(p_a\cdot t_{ref}\right)(\frac{\sigma_3}{p_a})^{n_2} \tag{19}$$

$$\eta^N=10^{K_3}\left(p_a\cdot t_{ref}\right)(\frac{\sigma_3}{p_a})^{n_3} \tag{20}$$

where t_{ref} is defined as the referenced time, which is equal to one hour. Here, K_1 , n_1, α, K_2, n_2, K_3 and n_3 are the new model parameters.

The values of E, G^K , η^K and η^N are continuously updated according to the stress state during numerical simulation. Details about the rheological model can be found in Xu *et al*. (2018).

This paper concerns the long-term deformation of geostructures caused by the creep of rockfills. The earthquake-induced deformation of geostructures is also of interest to researchers (e.g., Javdanian and Pradhan 2019, Javdanian *et al*. 2020, 2023, Shakarami *et al.* 2019).

4. Validation of the proposed back-analysis method

4.1 Numerical problem

In this section, a cross section of Jiuzhai-Huanglong Airport embankment is analyzed to investigate the accuracy and computational efficiency of the proposed method. The airport was constructed on the mountainous area of Sichuan Province in southwestern China, with a runway of 3400 m long. Dynamic compaction was the main construction method, and the total volume of rockfill is 2.76×10^7 m^3. The embankment was constructed on a slope, and the maximum height of the embankment is 90 m. Thus the long-term deformation and stability is of great concern.

The numerical simulation is performed with the finite difference program FLAC2D (Itasca 2005). The numerical mesh is shown in Fig. 3(a). The bedrock is modeled as a linear elastic material with a Young's modulus of 30 GPa and a Poisson's ratio of 0.3. The limestone rockfill is simulated using the rheological model described in Section 3. The construction process is simulated in six steps, and the timeline is displayed in Fig. 3(b). Steps 1-5 simulates the construction of the high rockfill embankment, and Step 6 simulates the preloading applied on the runway area.

4.2 Accuracy and computational efficiency of the proposed method

To make a quantitative evaluation of the accuracy of the proposed method, field monitoring data are not used here, since the exact solution of the model parameters is unknown. Instead, specified parameters (i.e., the exact solution) are pre-given, and the corresponding calculation results are taken as the "in-situ" monitoring data. By comparing the satisfactory solution obtained from back-analysis with the exact solution, the accuracy of the proposed method can be clearly assessed.

Two parameters are chosen for back analysis, so that the convergence process of the back-analysis can be graphically demonstrated, which would help the readers to understand the proposed method. Here K_1 and K_2 are selected as the

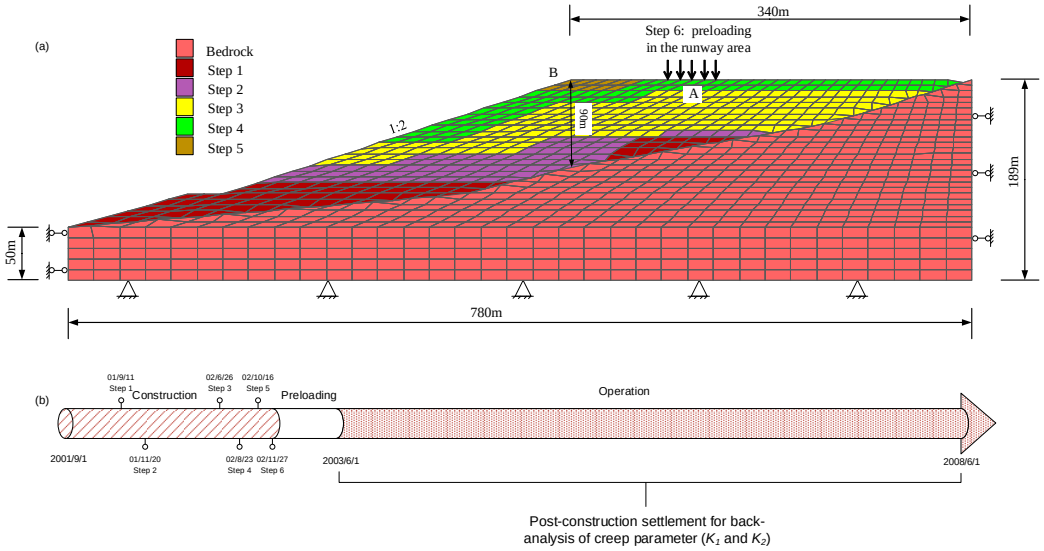

Fig. 3 The cross section of Jiuzhai-Huanglong Airport embankment: (a) numerical mesh; and (b) timeline for the back-analysis procedure

Table 1 Parameters of the rheological model for Example A and Example B

K	n	R_f	φ_0	$\Delta\varphi$	n_1	α	n_2	K_3	n_3
800	0.50	0.90	44.0	8.20	0.75	0.8	0.75	7.80	0.75

illustrative parameters since they have significant effects on the long-term deformation of the high embankments. Thus, $\mathbf{p}=[p_1, p_2]^{\mathrm{T}}$, in which $p_1 = K_1$ and $p_2 = K_2$. Two examples (i.e., Example A and Example B) with different exact solutions are used to investigate the robustness of the proposed method. The other nine model parameters are listed in Table 1. The convergence tolerance (F_{ct}) and the fitting tolerance (R_{fi}) are set to be 2% and 90%, respectively.

Example A

The exact solution of Example A is assumed to be K_1=1.6 and K_2=6.0. By performing numerical simulation with these two parameters, the settlement- time curves at Point A and Point B are obtained and assumed as the "in-situ" monitoring data. Point A and Point B are located at the mid of the runway and the top of the slope, respectively, as shown in Fig. 3(a). The detailed back-analysis procedure is presented as follows.

Stage 1: Improved weighted average method

Figure 4a shows the results of Stage 1, i.e., the improved weighted average method, which are obtained through the following four steps.

Step 1: Creating the calculation samples

Based on engineering experience, the initial region of K_1 and K_2 is assumed as [1.1, 1.8] and [5.2, 6.3], respectively. Thus, $\mathbf{p}_{\mathrm{c}}^{(0)}=\left[K_{1,\mathrm{c}}^{(0)}, K_{2,\mathrm{c}}^{(0)}\right]^{\mathrm{T}}=[1.45, 5.75]^{\mathrm{T}}$ and $\Delta\mathbf{p}^{(0)}=\left[\Delta K_1^{(0)}, \Delta K_2^{(0)}\right]^{\mathrm{T}}=[0.35, 0.55]^{\mathrm{T}}$. As mentioned in Section 2.2.1, nine calculation samples are created to construct the initial exploration region, which are represented as orange circles in Fig. 4(a).

Step 2: Calculating u_i for each calculation sample

The values of $F(\mathbf{p})$ of the nine calculation samples are calculated, and the corresponding weight u_i are derived according to Eq. (4), as shown in Table 2.

Step 3: Calculating $\mathbf{p}_{\mathrm{opt}}^{(0)}$

According to Eq. (5), the optimal solution of the improved weighted average method is obtained as $\mathbf{p}_{\mathrm{opt}}^{(0)}=[1.470, 6.003]^{\mathrm{T}}$ and $F\left(\mathbf{p}_{\mathrm{opt}}^{(0)}\right)$ = 20.05%, which is greater than F_{ct} (2%). Thus, Step 4 is performed.

Step 4: Determining the first exploration region

$\mathbf{p}_{\mathrm{opt}}^{(0)}$ is the center of the first exploration region ($\mathbf{p}_{\mathrm{c}}^{(1)}$=$\mathbf{p}_{\mathrm{opt}}^{(0)}$). According to Eq. (6), the ranges of the two parameters are

$$\Delta K_1^{(1)}=\Delta K_1^{(0)}\left(\frac{F\left(\mathbf{p}_{\mathrm{c}}^{(1)}\right)}{F\left(\mathbf{p}_{\mathrm{c}}^{(0)}\right)}\right),\quad \Delta K_2^{(1)}=\Delta K_2^{(0)}\left(\frac{F\left(\mathbf{p}_{\mathrm{c}}^{(1)}\right)}{F\left(\mathbf{p}_{\mathrm{c}}^{(0)}\right)}\right) \tag{21}$$

$\Delta\mathbf{p}^{(1)}=\left[\Delta K_1^{(1)}, \Delta K_2^{(1)}\right]^{\mathrm{T}}=[0.099, 0.156]^{\mathrm{T}}$. Therefore, the first exploration region (Region$^{(1)}$) for the next stage (i.e., adaptive RSM) is [1.371, 1.569] and [5.847, 6.159] for K_1 and K_2, respectively.

Stage 2: Adaptive response surface method

Two iterations are preformed at Stage 2 using the adaptive RSM before the satisfactory solution of Example A is obtained, as displayed in Fig. 4(b).

First iteration

Step 1: Determining the exploration region

In the first iteration (i.e., m=1), the exploration region provided by the improved weighted average method is

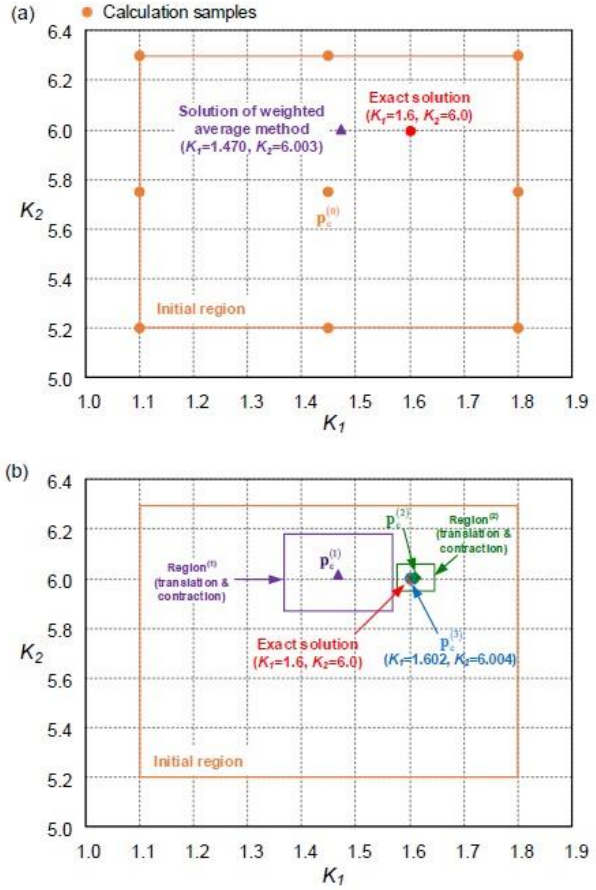

Fig. 4 Procedure of the hybrid back-analysis for Example A: (a) Stage1, the improved weighted average method; and (b) Stage 2, the adaptive RSM

Table 2. Calculation samples constructing the exploration region of the improved weighted average method for Example A

No.	K_1	K_2	$F(\mathbf{p})$ (%)	u_i (%)
1	1.100	5.200	378.686	1.382
2	1.100	6.300	20.911	25.029
3	1.800	5.200	58.211	8.991
4	1.800	6.300	52.281	10.011
5	1.450	5.750	70.801	7.392
6	1.100	5.750	156.122	3.352
7	1.450	5.200	174.212	3.004
8	1.800	5.750	31.726	16.497
9	1.450	6.300	21.501	24.342
$\mathbf{p}_{\text{opt}}^{(0)}$	1.4701	6.0030	20.050	

[1.371, 1.569] for K_1 and [5.847, 6.159] for K_2. Thus, $\mathbf{p}_{\text{c}}^{(1)}=[1.470, 6.003]^{\text{T}}$ and $\Delta\mathbf{p}^{(1)}=[0.099, 0.156]^{\text{T}}$.

Step 2: Creating the calculation samples

Nine calculation samples are created and the corresponding $F(\mathbf{p})$ are derived, as shown in Table 3.

Table 3 Calculation samples constructing the exploration region in the first iteration of the adaptive RSM for Example A

Natural Variables		Coded Variables		$F(\mathbf{p})$(%)
K_1	K_2	x_1	x_2	
1.3710	5.8473	-1.000	-1.000	70.710
1.3710	6.1588	-1.000	1.000	17.151
1.5692	5.8473	1.000	-1.000	25.318
1.5692	6.1588	1.000	1.000	12.736
1.4701	6.0030	0.000	0.000	20.050
1.3299	6.0030	-1.414	0.000	44.888
1.6102	6.0030	1.414	0.000	2.193
1.4701	5.7828	0.000	-1.414	59.663
1.4701	6.2233	0.000	1.414	11.590

Step 3: Constructing the response surface in the current iteration

The natural variables are coded to the usual [-1, 1] interval, i.e.

$$x_1=\frac{K_1-1.470}{1.569-1.371} \text{ and } x_2=\frac{K_2-6.003}{6.159-5.847} \tag{22}$$

The coded variables of the nine calculation samples are listed in Table 3. Therefore, the response surface is obtained

$$F^{(1)}(\mathbf{x})=0.2-0.138x_1-0.168x_2+0.022x_1^2 +0.102x_1x_2+0.083x_2^2 \tag{23}$$

Because $R^2=92.1\%$ of Eq. (23) is greater than the fitting tolerance (R_{fi}=90%), the adaptive RSM is continued.

Step 4: Identifying the optimal solution in the current iteration

Eq. (23) is re-written in matrix notation as

$$F^{(1)}(\mathbf{x})=\beta_0^{(1)}+\mathbf{x}^{\text{T}}\mathbf{b}^{(1)}+\mathbf{x}^{\text{T}}\mathbf{B}^{(1)}\mathbf{x} \tag{24}$$

where

$$\mathbf{x}=\begin{bmatrix}x_1\\x_2\end{bmatrix},\ \mathbf{b}^{(1)}=\begin{bmatrix}-0.138\\-0.168\end{bmatrix} \text{ and } \mathbf{B}^{(1)}=\begin{bmatrix}0.022 & 0.051\\0.051 & 0.083\end{bmatrix}$$

Then, the solution that has the minimum value of $F^{(1)}(\mathbf{x})$ is

$$\mathbf{x}_{\text{RSM}}^{(1)}=-\frac{1}{2}\left[\mathbf{B}^{(1)}\right]^{-1}\mathbf{b}^{(1)}=\begin{bmatrix}-1.845\\2.159\end{bmatrix} \tag{25}$$

Finally, the coded variables are transformed back into the natural variables, i.e., $\mathbf{p}_{\text{RSM}}^{(1)}=[1.287, 6.339]^{\text{T}}$ and the $F\left(\mathbf{p}_{\text{RSM}}^{(1)}\right)$ value is found to be 60.2%. By comparing $F\left(\mathbf{p}_{\text{RSM}}^{(1)}\right)$ with those in Table 3, the optimal solution is obtained as $\mathbf{p}_{\text{opt}}^{(1)}=[1.610,, 6.003]^{\text{T}}$ and $F\left(\mathbf{p}_{\text{opt}}^{(1)}\right)$ =2.193%, which is still greater than F_{ct} =2%. Thus, the second iteration is required.

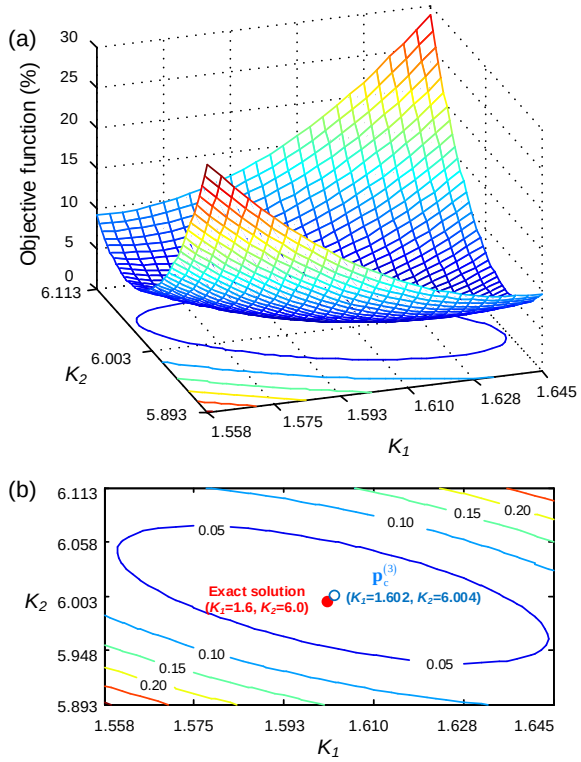

Fig. 5 Contour plot of the response surface in the second iteration of the adaptive RSM for Example A: (a) in a 3D view; and (b) in K_1 _ K_2 space

Table 4 Calculation samples constructing the exploration region in the second iteration of the adaptive RSM for Example A

Natural Variables		Coded Variables		$F(\mathbf{p})$(%)
K_1	K_2	x_1	x_2	
1.5752	5.9480	-1.000	-1.000	11.075%
1.5752	6.0580	-1.000	1.000	3.295%
1.6452	5.9480	1.000	-1.000	5.487%
1.6452	6.0580	1.000	1.000	14.015%
1.6102	6.0030	0.000	0.000	2.193%
1.5607	6.0030	-1.414	0.000	6.913%
1.6597	6.0030	1.414	0.000	11.504%
1.6102	5.9253	0.000	-1.414	6.572%
1.6102	6.0808	0.000	1.414	10.421%

Second iteration

Similar to the first iteration, the second iteration of the adaptive RSM is conducted in four steps. The detailed process is not presented here, but the basic information is presented in Table 4. The corresponding response surface is

$$F^{(2)}(\mathbf{x}) = 0.022 + 0.145x_1 + 0.008x_2 + 0.034x_1^2 + 0.041x_1x_2 + 0.031x_2^2 \quad (26)$$

where $R^2 = 97.3\%$ of Eq. (26) is greater than $R_{ft} = 90\%$. The optimal solution is $\mathbf{p}_{\text{opt}}^{(2)} = [1.602, 6.004]^{\text{T}}$ and $F\left(\mathbf{p}_{\text{opt}}^{(2)}\right)$ =0.92%, which is less than F_{ct} =2%. Thus, $\mathbf{p}_{\text{opt}}^{(2)}$ is the satisfactory solution for Example A, i.e., K_1=1.602 and K_2=6.004, which is very close to the exact solution (K_1=1.6 and K_2=6.0).

The response surface of Eq. (26) is shown in Fig. 5(a), which indicates that K_1 has more significant effect on the objective function than K_2. In addition, the contour plot of the response surface (Fig. 5(b)) reveals that the satisfactory solution $\mathbf{p}_{\text{opt}}^{(2)}$ is very close to the pre-given "exact solution". Fig. 6 shows the convergence process of the settlement-time curves for Example A, obtained with parameters at the center of each exploration region. The numerical results approach the "in-situ" monitoring data with the translation of the exploration region.

Example B

For Example B, another set of exact solution is adopted, i.e., K_1=1.3 and K_2=5.4 . To facilitate comparison, the initial region is chosen as the same as that in Example A.

Figs. 7(a) and 7(b) schematically shows the convergence path during Stage 1 (the improved weighted average method) and Stage 2 (the adaptive RSM), respectively. Again, the numerical results approach the "in-situ" monitoring data quickly with the translation of the exploration region, and the satisfactory solution (K_1 =1.303, K_2 =5.387) is obtained via two iterations, which is also very close to the exact solution. Figure 8 displays the convergence process of the settlement-time curve for Example B.

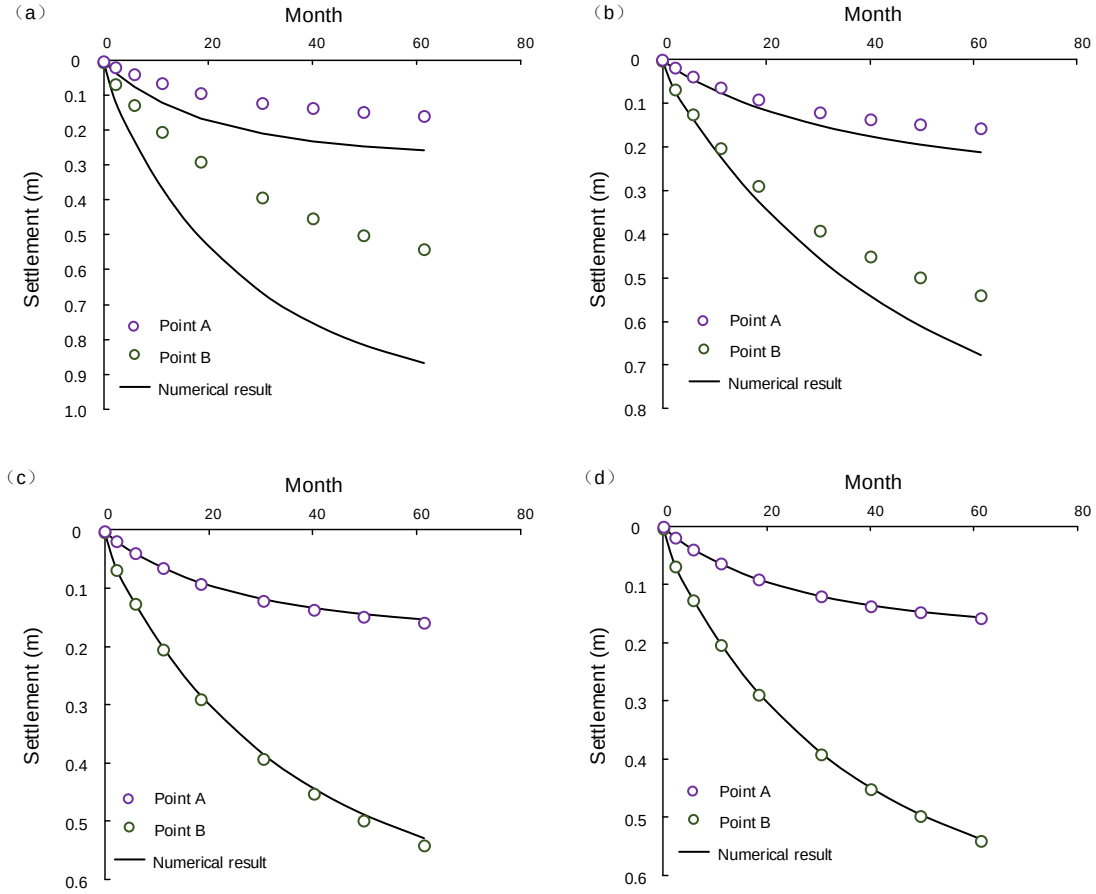

Fig. 6 Convergence process of settlement-time curves for Example A, obtained with parameters at the center of each exploration region: (a) $\mathbf{P}_c^{(0)}$, (b) $\mathbf{P}_c^{(1)}$, (c) $\mathbf{P}_c^{(2)}$ and (d) $\mathbf{P}_c^{(3)}$, compared with monitoring data

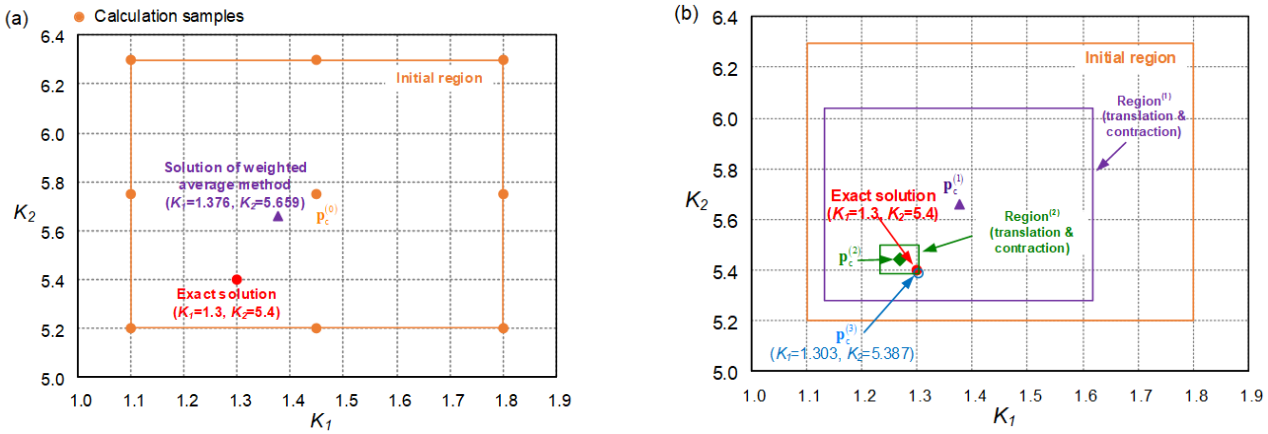

Fig. 7 Procedure of the hybrid back-analysis for Example B: (a) Stage1, the improved weighted average method; and (b) Stage 2, the adaptive RSM

Figs. 9(a) and 9(b) compare the $F(\mathbf{p})$ values at the center of the exploration region against the number of translations of the exploration region for Example A and Example B, respectively. Although the exact solutions of the two examples are very different, satisfactory solutions are obtained via only three translations. To make comparison, we performed back-analysis on the same problem using the conventional Response Surface Method, which took much longer computation time (results not shown here).

5. Case study of the Maotai Airport embankment

Maotai Airport is located in the mountainous area of Guizhou Province in southwestern China. The total length of the airport runway is 2600 m. The construction of the high rockfill embankment began in March 2015 and was completed at the end of December 2015, which lasted only nine months. The volume of excavation and filling was 1.65×10^7 m^3 and 1.81×10^7 m^3, respectively. The major

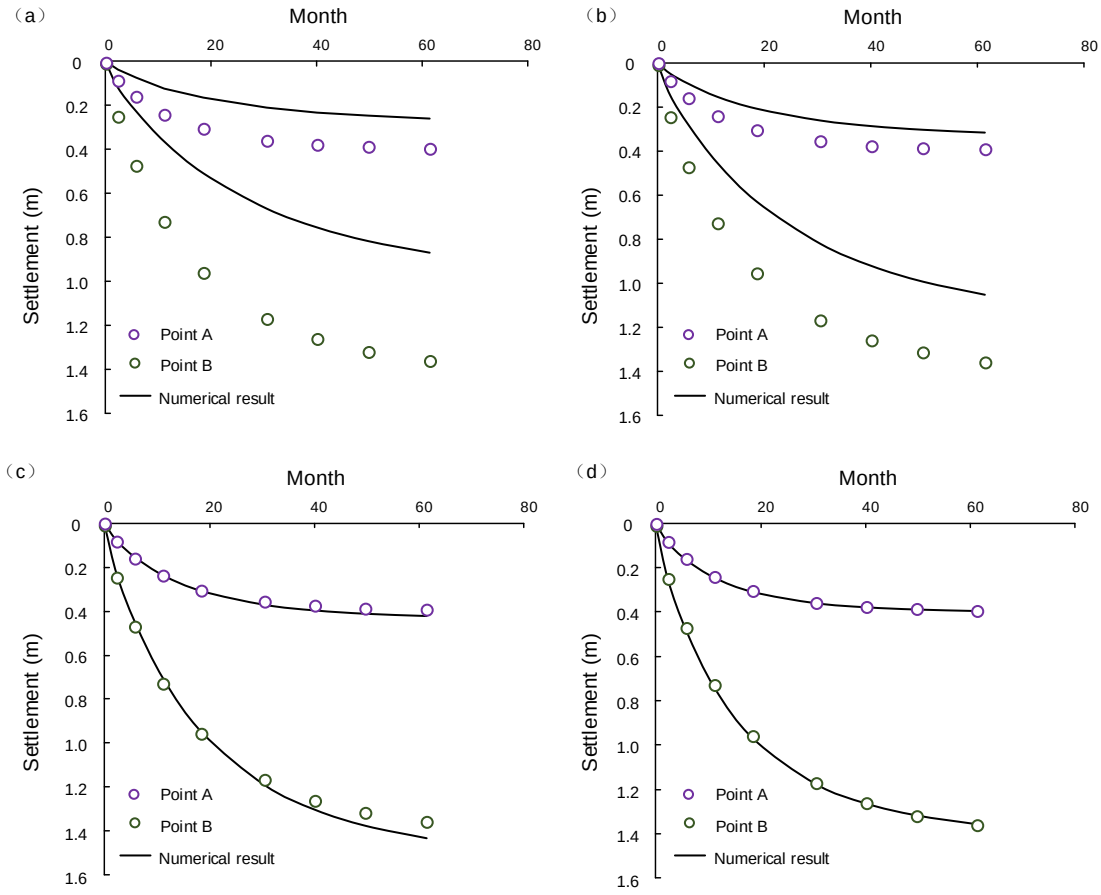

Fig. 8 Convergence process of the settlement-time curves for Example B, obtained with parameters at the center of each exploration region: (a) $\mathbf{P}_c^{(0)}$, (b) $\mathbf{P}_c^{(1)}$, (c) $\mathbf{P}_c^{(2)}$ and (d) $\mathbf{P}_c^{(3)}$, compared with monitoring data

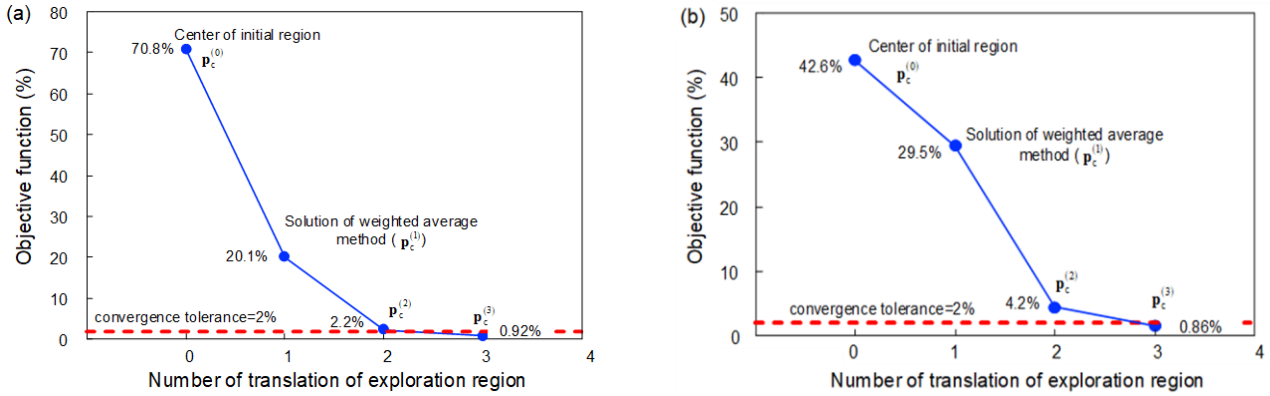

Fig. 9 Values of the objective function at the center of each exploration region for (a) Example A; and (b) Example B

construction materials were Dolomite rockfills, and dynamic compaction was carried out with a compaction energy level of 3000 kN*m. The maximum heights of the embankment is 56 m. Fig. 10(a) shows the high embankment during construction, and Fig. 10(b) shows an aerial view just after the construction of the runway.

A typical cross section of Maotai Airport (Fig. 11(a)) is modelled to predict the long-term deformation using the proposed back-analysis method. The bedrock is simulated with a linear elastic model, with a Young's modulus of 30 GPa and a Poisson's ratio of 0.3. The rockfill is simulated using the rheological model described in Section 3. The construction process is simplified into 7 steps, and the timeline is displayed in Fig. 11(b).

Settlement was measured at different locations, and the in-situ monitoring data of C11 (above the runway) and T10 (at the slope) are used in the back-analysis. K_1, K_2 and K_3 are selected as the unknown model parameters to be identified, as the other parameters have relatively minor influence on the long-term deformation. Thus, $\mathbf{p} = [p_1, p_2, p_3]^T$, in which $p_1 = K_1$, $p_2 = K_2$ and $p_3 = K_3$.

(a) During construction of the high rockfill embankment (b) After the construction of the runway

Fig. 10 Aerial view of the Maotai Airport embankment from unmanned drone

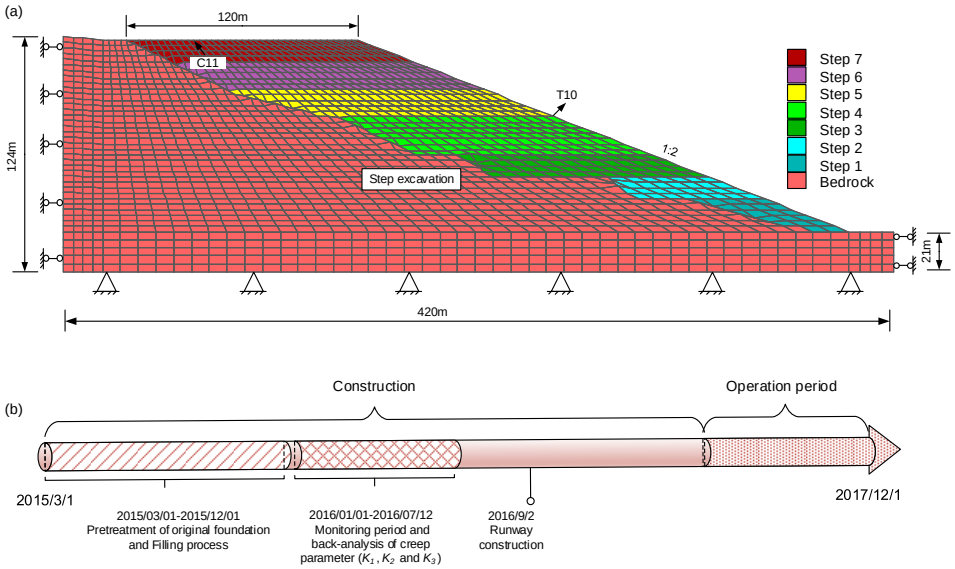

Fig. 11 The Maotai Airport embankment: (a) numerical mesh; and (b) timeline for the back-analysis procedure

Table 5 Parameters of the rheological model for the Maotai Airport embankment

K	n	R_f	φ_0	$\Delta\varphi$	n_1	α	n_2	n_3
1120	0.20	0.90	49.6	8.30	0.7	0.8	0.7	0.7

The other nine model parameters are listed in Table 5. The convergence tolerance (F_{ct}) and fitting tolerance (R_{ft}) are set to 5% and 90%, respectively.

A summary of the hybrid back-analysis is presented in Table 6. The values of $F(\mathbf{p})$ at the center of the exploration regions are plotted against the number of translation of the exploration region in Fig. 12, which show $F(\mathbf{p})$ decreases quickly with the translation. Fig. 13 displays the convergence process of the settlement-time curve for the Maotai Airport, showing that the numerical results gradually approach the in-situ monitoring data and the satisfactory results are finally achieved in Fig. 13(f).

The satisfactory solution is used to make practical prediction about the settlement of the Maotai Airport during the long-term operation period, as shown in Fig. 14. The settlement rates of the two monitoring points (C11 and T10) decrease with time and became insignificant during the operation period.

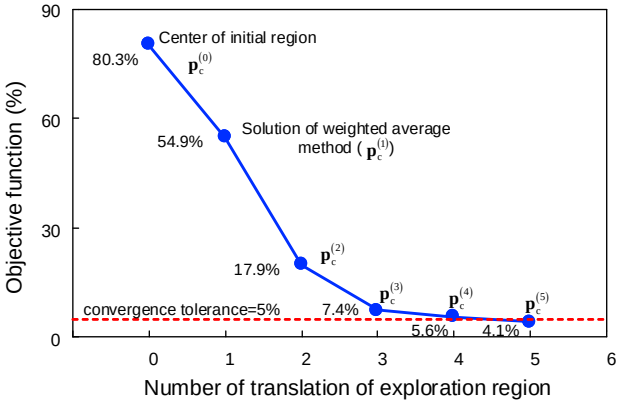

Fig. 12 Values of the objective function at the center of each exploration region for the Maotai Airport embankment

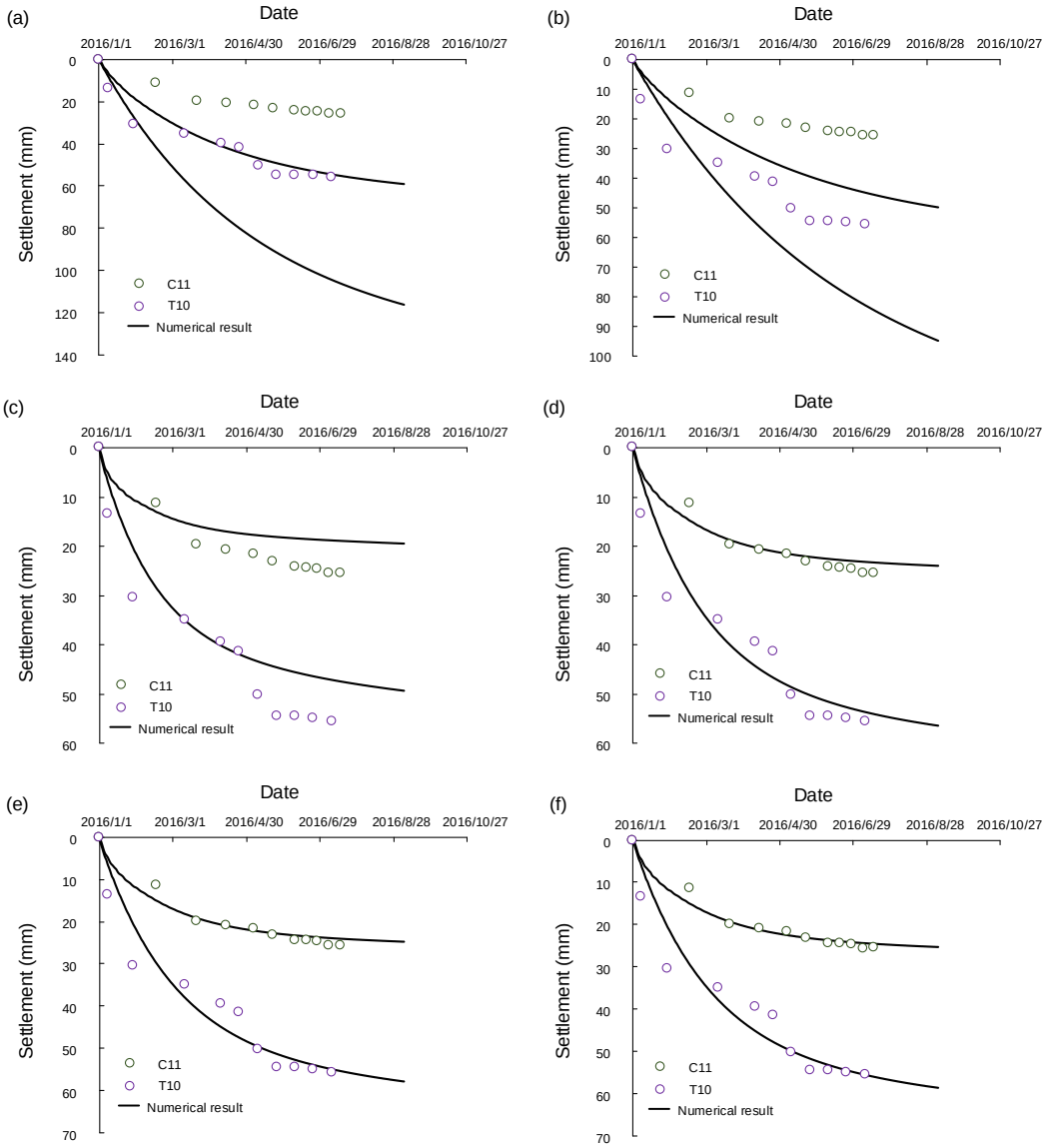

Fig. 13 Convergence process of settlement-time curves for Maotai Airport embankment, obtained with parameters at the center of each exploration region: (a) $\mathbf{P}_c^{(0)}$, (b) $\mathbf{P}_c^{(1)}$, (c) $\mathbf{P}_c^{(2)}$, (d) $\mathbf{P}_c^{(3)}$, (e) $\mathbf{P}_c^{(4)}$ and (f) $\mathbf{P}_c^{(5)}$ compared with monitoring data

Table 6 Summary of the exploration regions of the hybrid back-analysis for the Maotai Airport embankment

m	$K_{1,c}^{(m)}$	$K_{2,c}^{(m)}$	$K_{3,c}^{(m)}$	$\Delta K_1^{(m)}$	$\Delta K_2^{(m)}$	$\Delta K_3^{(m)}$	$F(\mathbf{p})$ (%)
0	1.5	5.0	7.4	0.35	0.5	0.6	80.27
1	1.518	5.145	7.403	0.239	0.342	0.410	54.91
2	1.758	4.803	7.814	0.078	0.112	0.134	17.94
3	1.721	4.874	7.824	0.035	0.050	0.060	7.350
4	1.714	4.888	7.823	0.035	0.050	0.060	5.533
5	1.712	4.895	7.822	-	-	-	4.127

m=0 for Stage1, and m=1~5 for Stage 2. When m=5, the satisfactory solution has been found

6. Conclusions

It is important to make reasonable prediction about the long-term deformation of high rockfill geostructures. However, the deformation is usually underestimated using the parameters obtained from laboratory tests due to different size effects, which make it necessary to identify parameters from in-situ monitoring data. This paper proposes a hybrid back-analysis method with a modified objective function defined for the time-dependent back-

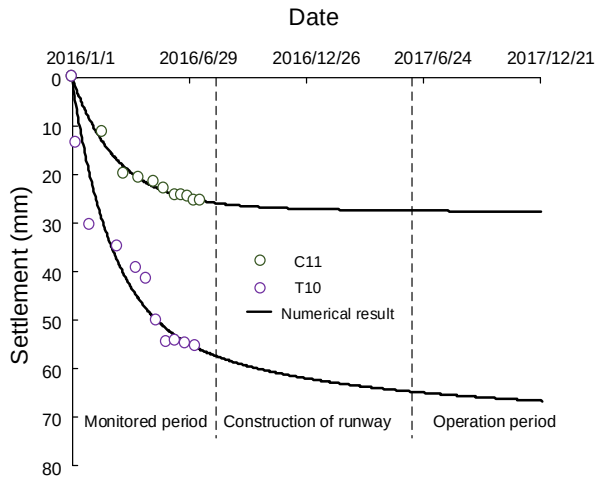

Fig. 14 Prediction of the settlement-time curves for the Maotai Airport embankment

analysis problem. In the first stage, an improved weighted average method is adopted to quickly narrow the search region and determine the first exploration region for the next stage. In the second stage, an adaptive response surface method is proposed to iteratively search for the satisfactory solution, with a technique that can adaptively consider the translation, contraction or expansion of the exploration region. The accuracy and computational efficiency of the proposed hybrid back-analysis method is demonstrated by back-analyzing the long-term deformation of two high embankments constructed for airport runways, in which the rockfill is modeled by a rheological model considering the influence of stress states on the creep behavior.

It should be noted that the number of parameters to be back-analyzed is chosen as 2 and 3 for those two high embankments for the ease of demonstration. It is possible to back-analyze more parameters using the proposed method, which requires more computational time.

Acknowledgments

The authors are grateful for the research support received from the National Natural Science Foundation of China (51978382) and the China 973 Program (2014CB047003).

References

Alonso, E., Romero, E. and Ortega, E. (2016), "Yielding of rockfill in relative humidity-controlled triaxial experiments", *Acta Geotechnica*, **11**, 455-477. https://doi.org/10.1007/s11440-016-0437-9.

Alonso, E., Tapias, M. and Gili, J. (2012), "Scale effects in rockfill behavior", *Géotechnique Lett.*, **2**, 155-160. https://doi.org/10.1680/geolett.12.00025.

Anhdan, L., Tatsuoka, F. and Koseki, J. (2006), "Viscous effects on the stress-strain behavior of gravelly soil in drained triaxial compression", *ASTM Geotech. Test J.*, **29**(4), 330- 340. https://doi.org/10.1520/GTJ12720.

Behnia, D., Ahangari, K., Noorzad, A. and Moeinossadat, S.R. (2013), "Predicting crest settlement in concrete face rockfill dams using adaptive neuro-fuzzy inference system and gene expression programming intelligent methods", *J. Zhejiang Univ. Sci. A*, **14**(8), 589-602. https://doi.org/10.1631/jzus.A1200301.

Calvello, M. and Finno, R.J. (2004), "Selecting parameters to optimize in model calibration by inverse analysis", *Comput. Geotech.*, **31**(5), 410-424. https://doi.org/10.1016/j.compgeo.2004.03.004.

Canizal, J., Castro, J., Costa, A.D., Sagaseta, C. and Sola, P. (2015), "High rockfill embankment for the extension of an airport main runway", *Proceedings of the 15th Pan-American Conference on Soil Mechanics and Geotechnical Engineering*, Buenos Aires, Argentina, December. https://doi.org/10.3233/978-1-61499-603-3-188.

Charles, J.A. (2008), "The engineering behavior of fill materials, the use, misuse and disuse of case histories", *Géotechnique*, **58**(7), 541-570. https://doi.org/10.1680/geot.2008.58.7.541.

Ducan, J. and Chang, C. (1970), "Nonlinear analysis of stress and strain in soils", *J. Soil Mech. Found. Division*, **96**(5), 1629-1652. https://doi.org/10.1061/JSFEAQ.0001458.

Finno, R.J. and Calvello, M. (2005), "Supported excavations: observational method and inverse modeling", *J. Geotech. Geoenviron. Eng.*, **131**(7), 826-836. https://doi.org/10.1061/(ASCE)1090-0241(2005)131:7(826).

Frossard, E., Hu, W., Dano, C. and Hicher, P. (2012), "Rockfill shear strength evaluation: a rational method based on size effects", *Geotechnique*, **62**(5), 415-427. https://doi.org/10.1680/geot.10.P.079.

Guan, Z., Jiang, Y., Tanabashi, Y. and Huang, H. (2008), "A new rheological model and its application in mountain tunneling", *Tunn. Undergr. Sp. Technol.*, **23**(3), 292-299. https://doi.org/10.1016/j.tust.2007.06.003.

Hong, J. and Xu, M. (2021), "Numerical investigation of the time size effect of high rockfill geostructures", *Transport. Geotech.*, **30**, 100613. https://doi.org/10.1016/j.trgeo.2021.100613.

Hu, W., Dano, C., Hicher, P.Y., Touzo, J.Y.L., Derkx, F. and Merliot, E. (2011), "Effect of sample size on the behavior of granular materials", *ASTM Geotech. Test. J.*, **34**(3), 186-197. https://doi.org/10.1520/GTJ103095.

Itasca. (2005), User's guide for FLAC version 5.0.

Javdanian, H. and Pradhan, B. (2019), "Assessment of earthquake-induced slope deformation of earth dams using soft computing techniques", *Landslides*, **16**(1), 91-103. https://doi.org/10.1007/s10346-018-1078-x.

Javdanian, H., Zarif Sanayei, H.R. and Shakarami, L. (2020), "A regression-based approach to the prediction of crest settlement of embankment dams under earthquake shaking", *Scientia Iranica*, **27**(2), 671-681. https://doi.org/10.24200/sci.2018.50483.1716.

Javdanian, H., Zarei, M. and Shams, G. (2023), "Estimating seismic slope displacements of embankment dams using statistical analysis and numerical modeling", *Model. Earth Syst. Environ.*, **9**, 389-396. https://doi.org/10.1007/s40808-022-01505-4.

Kermani, M., Konrad, J.M. and Smith, M. (2017), "An empirical method for predicting post-construction settlement of concrete face rockfill dams", *Can. Geotech. J.*, **54**(6), 755-767. https://doi.org/10.1139/cgj-2016-0193.

Ledesma, A., Gens, A. and Alonso, E.E. (1996), "Estimation of parameters in geotechnical back analysis—I. Maximum likelihood approach", *Comput. Geotech.*, **18**(1), 1-27. https://doi.org/10.1016/0266-352X(95)00021-2.

Lee, D.M. (1992), *The angles of friction of granular fills*, PhD dissertation, Canbridge University.

Mcdowell, G.R. and Bolton, M.D. (1998), "On the micromechanics of crushable aggregates", *Geotechnique*, **48**(5), 667-679. https://doi.org/10.1061/JSFEAQ.0000958.

Oyejola, B.A. and Nwanya, J.C. (2015), "Selecting the right

central composite design", *Int. J. Stat. Appl.*, **5**(1), 21-30. https://doi:10.5923/j.statistics.20150501.04.

Nagahara, H., Fujiyama,T., Ishiguro, T. and Ohta, H. (2004), "FEM analysis of high airport embankment with horizontal drains", *Geotext. Geomembranes*, **22**(2), 49-62. https://doi.org/10.1016/S0266-1144(03)00051-7.

Nasiri, F., Javdanian, H. and Heidari, A. (2020), "Seismic response analysis of embankment dams under decomposed earthquakes", *Geomech. Eng.*, **21**(1), 35-51. https://doi.org/10.12989/gae.2020.21.1.035.

Park, D. and Park, E.S. (2015), "Inverse parameter fitting of tunnels using a response surface approach", *Int. J. Rock Mech. Min. Sci.*, **77**, 11-18. https://doi.org/10.1016/j.ijrmms.2015.03.026.

Pichler, B., Lackner, R. and Mang, H.A. (2003), "Back analysis of model parameters in geotechnical engineering by means of soft computing", *Int. J. Numer. Method. Eng.*, **57**(14), 1943-1978. https://doi.org/10.1002/nme.740.

Qin, X., Gu, C., Shao, C., Chen, Y., Valleji, L. and Zhao, E. (2020), "Safety evaluation with observational data and numerical analysis of Langyashan reinforced concrete face rockfill dam", *Bull. Eng. Geol. Environ.*, **79**, 3497-3515. https://doi.org/10.1007/s10064-020-01790-2.

Rahmania, H. and Panah A.K. (2020), "Effect of particle size and saturation conditions on the breakage factor of weak rockfill materials under one-dimensional compression testing", *Geomech. Eng.*, **21**(4), 315-326. https://doi.org/10.12989/gae.2020.21.4.315.

Sarabia, L.A. and Ortiz, M.C. (2020), *Response Surface Methodology*, Comprehensive Chemometrics. https://doi.org/10.1016/B978-044452701-1.00083-1.

Shakarami, L., Javdanian, H., Zarif Sanayei, H.R. and Shams, G. (2019), "Numerical investigation of seismically induced crest settlement of earth dams", *Model. Earth Syst. Environ.*, **5**, 1231-1238. https://doi.org/10.1007/s40808-019-00624-9.

Song, E., Zheng, T. and Kong, Y. (2018), "Tentative investigation of structure size effect of high-filled geotechnical structures", *Proceedings of the China-Europe Conference on Geotechnical Engineering*, 1726-1729. https://doi.org/10.1007/978-3-319-97115-5_179.

Soriano, A. and Sanchez, F.J. (1999), "Settlements of railroad high embankments", *Proceedings of the 12th European Conference on Soil Mechanics and Geotechnical Engineering*, 1885-1890.

Sukkarak, R., Pramthawee, P., Jongpradist, P., Kongkitkul, W. and Jamsawang, P. (2018), "Deformation analysis of high CFRD considering the scaling effects", *Geomech. Eng.*, **14**(3), 211-224. https://doi.org/10.12989/gae.2018.14.3.211.

Tapias, M., Alonso, E.E. and Gili, J.A. (2015), "A particle model for rockfill behavior", *Geotechnique*, **65**(12), 975-994. https://doi.org/10.1680/jgeot.14.P.170.

Wang, Z., Li, Y. and Shen, R.F. (2007), "Correction of soil parameters in calculation of embankment settlement using a BP network back-analysis model", *Eng. Geol.*, **91**(2-4), 168-177. https://doi.org/10.1016/j.enggeo.2007.01.007.

Xu, M., Song, E. and Cao, G. (2009), "Compressibility of broken rock-fine grain soil mixture", *Geomech. Eng.*, **1**(2). https://doi.org/10.12989/gae.2009.1.2.169.

Xu, M., Song, E. and Chen, J. (2012), "A large triaxial investigation of the stress-path-dependent behavior of compacted rockfills", *Acta Geotechnica*, **7**(3), 167-175. https://doi.org/10.1007/s11440-012-0160-0.

Xu, M., Song, E. and Jin, D. (2017), "A strain hardening model for the stress-path-dependent shear behavior of rockfills", *Geomech. Eng.*, **13**(5), 743-756. https://doi.org/10.12989/gae.2017.13.5.743.

Xu, M., Jin, D., Song, E. and Shen, D. (2018), "A rheological model to simulate the shear creep behavior of rockfills considering the influence of stress states", *Acta Geotechnica*, **13**(6), 1313-1327. https://doi.org/10.1007/s11440-018-0716-8.

Xu, M., Jin D., Song, E., Shen, Z., Yang, Z. and Fu, J. (2019), "Full-scale creep test and back-analysis of the long-term settlement of heavy-loaded shallow foundations on a high rockfill embankment", *Comput. Geotech.*, **115**, 103156. https://doi.org/10.1016/j.compgeo.2019.103156.

Yao, Y.P., Qi, S.J., Che, L.W., Chen, J., Han, L.M. and Ma, X.Y. (2018), "Postconstruction settlement prediction of high embankment of silty clay at Chengde Airport based on one-dimensional creep analytical method: case study", *Int. J. Geomech.*, **18**(7), 05018004. https://doi.org/10.1061/(ASCE)GM.1943-5622.0001191.

Yao, Y., Huang, J., Wang, N., Luo, T. and Han, L. (2020), "Prediction method of creep settlement considering abrupt factors", *Transport. Geotech.*, **22**, 100304. https://doi.org/10.1016/j.trgeo.2019.100304.

Zhao, H., Ru, Z. and Yin, S. (2015), "A practical indirect back analysis approach for geomechanical parameters identification", *Mar. Georesour. Geotec.*, **33**(3), 212-221. https://doi.org/10.1080/1064119X.2013.836258.

Zhou, W., Li, S. L., Ma, G., Chang, X.L., Cheng, Y.G. and Ma, X. (2016), "Assessment of the crest cracks of the Pubugou rockfill dam based on parameters back analysis", *Geomech. Eng.*, **11**(4), 571-585. https://doi.org/10.12989/gae.2016.11.4.571.

Zhou, X., Ma, G. and Zhang, Y. (2019), "Grain size and time effect on the deformation of rockfill dams: a case study on the Shuibuya CFRD", *Geotechnique*, **69**(7), 606-619. https://doi.org/10.1680/jgeot.17.P.299.

Zhou M., Shadabfar M., Huang, H., Leung Y.F. and Uchida S. (2022), "Efficient back analysis of multiphysics processes of gas hydrate production through artificial intelligence", *Fuel*, **323**, 124162. https://doi.org/10.1016/j.fuel.2022.124162.

CC